Analysis of the source scanning algorithm with a new P-wave picker

J. Zahradník · J. Janský · V. Plicka

Abstract We analyze the location of earthquakes in near regional networks using complete seismic records. The method is based on the source scanning algorithm (SSA) of Kao and Shan (2004), but similarly to Grigoli et al. (2013), seismograms are substituted by a P-wave picker trace. The picker traces in a network are repeatedly stacked using grid of trial source positions, and hypocenter is identified with the point providing the best stack (the largest brightness). The first innovation of this paper is a new picker, measuring the ratio of the summed absolute values of seismogram in the right and left part of a moving time window, the RPA/LPA picker. The brightness maps based on this picker are clearer than those based on the STA/LTA picker. The second innovation is a simple theoretical model of the brightness maps. It makes it easy to identify how individual stations contribute to form the brightness spot. It is shown on synthetic tests that the performance of the method depends on focal mechanism, progressively improving from normal to reverse and strike-slip events. The method is successfully applied to four events of different mechanisms and depths, recorded at different ranges of epicentral distance by either broad-band sensors or accelerographs. The events have been located close to previously published epicenters. The brightness maps provide an estimate of the relative uncertainty of the (non-linear) location problem. The uncertainty estimate is also applicable without measured arrival times, "without earthquakes", thus useful when designing or upgrading seismic networks for better location performance.

1 Introduction

Huge and further growing amounts of seismic data require fully automated data processing. Most of the automatic location methods imitate the traditional approach: they use a picker, extract P- or P- and S-wave arrival times, and invert them for hypocenter position and origin time by a linearized approach. The limitations of such an approach are obvious: (i) emergent onsets are lost, or their representation by a single temporal value is inaccurate, (ii) uncertainty estimate of the location does not reflect non-linearity of the problem, and (as a rule) it ignores effects of the inaccurate velocity model. (iii) Association of phases is difficult if two or more events occurred close to each other almost simultaneously. Therefore, alternative approaches are being introduced.

The source scanning algorithm (SSA) has been developed since 2004 (e.g., Kao and Shan, 2004, 2007; Kao et al., 2009). For a good literature overview of the

J. Zahradník (✉) · J. Janský · V. Plicka
Department of Geophysics, Faculty of Mathematics and Physics, Charles University in Prague,
Ke Karlovu 3, 12116 Prague 2, Czech Republic
e-mail: Jiri.Zahradnik@mff.cuni.cz

preceding and following developments, see, Liao et al. (2012) and Langet et al. (2014). The basic idea of SSA is simple: seismograms in a station network can be stacked using theoretical travel times, calculated with a given (e.g., 1D or 3D) velocity model and an assumed point-source position. A set of trial source positions covering the scanned region of interest is grid searched, and hypo-center is identified with the position(−s) producing the largest value of the stack (so-called brightness). Effects of noise and imperfect knowledge of the velocity model can be partly suppressed by considering a weighted contribution from neighboring points within a chosen time window. The method is appealing because it makes use of waveforms, without requiring phase-arrival picking. It is therefore applicable even to events with unclear arrivals. As such, the method was reported useful for tremors, including their continuous monitoring. However, tremor locations could not be validated by any other method, thus leaving success of the SSA location basically untested. Therefore, a fundamental (not yet fully answered) question is whether SSA is applicable to earthquakes, and if it is competitive with the standard location approaches.

To answer the question, the objective of this paper is to analyze performance of the SSA method both on synthetic tests and real data, and possibly improve it by certain innovations. We shall investigate various definitions of brightness, trying to improve the sharpness of the brightness maps. We shall also provide a simple theoretical model of the brightness filed, helping to understand the role of individual stations and to evaluate the relative location uncertainty. Bulk of the paper (all synthetic tests and one real data application) is devoted to the January 18, 2010, Mw 5.3 Efpalio earthquake, Greece. The location and focal mechanism of this earthquake were thoroughly investigated by Sokos et al. (2012) and Janský et al. (2012). In less detail, the performance of the method is demonstrated also for three other earthquakes, covering a broad range of focal mechanisms, depths, and epicentral distances.

2 Method

We focus on P-waves in near-regional networks. As such, the P-wave groups have their amplitude and form strongly variable from station to station, due to focal mechanism and structural effects. Then, direct stacking of seismograms, without prior pre-processing of the P-wave group, is not viable. Therefore, following Grigoli

et al. (2013), we apply a picker to each seismogram, and, instead of seismograms, we stack the (time varying) picker traces. As an innovation, we compare the STA/LTA picker with a new one, called RPA/LPA. The S waves are not dealt with in this paper at all.

Pickers Standard STA/LTA (short time average versus long time average) picker consists of applying two running-average windows, both situated to the left of the current point t of the time series $s(t)$, and having common their right-hand edge. The two windows have an unequal number of samples, $J < K$, where J and K refer to the short and long time average, respectively. In this paper, we systematically use $J = K/4$. The picker trace is denoted $T(t)$, or, to emphasize its functional dependence on the (absolute-valued) time series s(t), the picker trace can also be denoted $T(s(t))$. Subscript of T will indicate the picker type.

$$T_{\text{STA/LTA}}(s(t)) = \frac{\frac{1}{J}\sum_{j=1}^{J} s(t-\tau_j)}{\frac{1}{K}\sum_{k=1}^{K} s(t-\tau_k)} \qquad (1)$$

The new picker of this paper, called RPA/LPA (right part average versus left part average) consists of applying two running-average windows of equal length (number of samples J), situated symmetrically with respect to the current point of the time series

$$T_{\text{RPA/LPA}}(s(t)) = \frac{\sum_{j=1}^{J} s(t+\tau_j)}{\sum_{j=1}^{J} s(t-\tau_j)} \qquad (2)$$

Stacking picker traces We start with absolute-valued non-normalized waveforms $w_n(t)$, at each station n= 1,2, … N. We apply a P-wave picker, $T_n(t) = T(w_n(t))$, normalize the picker traces $T_n(t)$ (i.e., we set their peak value equal to unity at each station), and we stack them repeatedly for all points m=1,2,…M of the trial-source grid. The stack $S_m(t)$ depends on time and on the trial source position:

$$S_m(t) = (1/N)\sum_{n=1}^{N} T_n(t + tt_{nm}) \qquad (3)$$

Here tt_{nm} denotes the (pre-calculated) travel time between m-th trial position of the source and n-th station. The following procedure may have two forms.

Space dependent brightness The time-dependent stack is maximized over time at any space grid point m to obtain the space-dependent brightness B_m

$$B_m = \max_t (S_m(t)) \qquad (4)$$

Note that, according to this definition, brightness values B_m at different spatial positions m are, in general, related to different times. Optimum hypocenter position is defined by $m = m_{opt}$ which maximizes B_m over all considered source positions. An alternative approach (later proven to be preferable) is the space-time dependent brightness of the next paragraph.

Space-time dependent brightness We introduce one more source parameter, the origin time, which is also grid searched: ot_i, i=1,2,...I. The space-time dependent brightness is defined as

$$B_m(ot_i) = S_m(t = ot_i) \qquad (5)$$

In this approach, the spatial variation of B_m is inspected separately for each trial origin time ot_i. In other words, instead of a single brightness x–y map, we have a series of such maps for varying ot_i. We speak about "animation" of the brightness field, composed of individual "snapshots".

We also compute $B_{opt}(ot_i) = \max_m (S_m(t = ot_i))$ and save the source position producing this maximization, $m_{opt} = m_{opt}(ot_i)$. This is the optimum space position of the source for a given trial origin time. Further, we seek the trial origin time ot_{opt} for which we obtain $\max_{ot} (B_{opt}(t = ot_i))$. The ot_{opt} value represents the resulting origin time. The resulting hypocenter position is at $m_{opt}(ot_{opt})$.

In both approaches, with- or without temporal variation, we are interested not only in the position of the maximum brightness, but also in the slightly smaller values (within a chosen threshold). These form a "bright spot" in the brightness map, reflecting a relative location uncertainty.

Obviously, the two approaches should in principle provide the same hypocenter, because both include maximization of the stack of the picker traces over time and space, only the order of the two maximizations is opposite. The space-dependent brightness (without the temporal evolution) is fast. The speedup with respect to the space-time brightness is proportional to the number of the trial values of the origin times. However, the space-time brightness is preferable: (i) The brightness maps are homogenous with respect to time (each map is related to a single trial time). (ii) The method implicitly provides also the origin time. (iii) In case of artifacts, i.e., spots of strong brightness, almost equal to its maximum value, these artifacts are better understandable from the temporal evolution of the brightness field. The space-time approach might have also some potential to detect source complexities, such as multiple nucleation points, but these aspects need a special investigation elsewhere.

As we have two pickers ($T_{STA/LTA}$ and $T_{RPA/LPA}$), we can compute the brightness in two different forms: $B_{STA/LTA}$ and $B_{RPA/LPA}$, respectively.

Source, stations, and velocity models Most tests of this paper are related to the Efpalio 2010 earthquake (event 1 in Tables 1 and 2). The selected source-station

Table 1 Previously determined parameters of studied events (UPSL)

Event no.	Date	Origin Time	Lat (°N)	Lon (°E)	Depth (km)	Agency	Strike/Dip/Rake (°)	Mo (Nm)	Mw	Agency
1	20100118	15:56:08.00	38.419	21.915	6.6	UPSL	102/55/−83	0.97e17	5.3	Sokos et al., 2012
2	20120613	19:27:31.31	38.044	21.566	18	UPSL	191/89/170	7.28e14	3.8	UPSL
3	20090406	01:32:40.40	42.342	13.380	8.3	ISIDE	127/50/−109	3.42e18	6.3	GCMT
4	20111023	10:41:20.00	38.689	43.466	19	Tr-KYH	248/36/60	6.40e19	7.2	GCMT

UPSL University of Patras, Seismological Laboratory

ISIDE Italian Seismological and Parametric Data Base

Tr-KYH Strong Motion Dta Base of Turkey

GCMT Global Centroid Moment Tensor Project

Table 2 Location results of the present paper

Event no.	OT increment (s)	NS increment (km)	EW increment (km)	Depth increment (km)	No. of stations	Type of record	Time step (s)	Picker window (s)	Velocity model
1	0.6	0	1	8[a]	12	Velocity	0.03	1	Fig. 1b
2	0.2	0	3	2[a]	6	Velocity	0.03	1	Novotný et al. 2001
3	1.0	0	0	1[a]	9	Velocity	0.01	1	Ameri et al. 2012
4	0.6	3	−4	−12	4	Acceleration	0.05	3	Gallovič et al. 2013

The location increments are expressed with respect to the location in Table 1.

[a] Poor depth resolution

configuration is shown in Fig. 1a. The epicentral distance ranges from 15 to 193 km. The Cartesian coordinate system has its origin in the epicenter found by Sokos et al. (2012). The horizontal x and y axes are positive toward East and North, respectively. The 1D velocity model adopted in this paper (Fig. 1b) is a simplified version of a model introduced by Sokos et al. (2012), based on the tomography results of Latorre et al. (2004). The P-wave velocity below Moho is 7.0 km/s (Rigo et al., 1996). Theoretical travel times are calculated by the ray method, including head waves from all velocity discontinuities (intra-crustal discontinuities and Moho); we used code ANG (author J. Janský, unpublished). The following study includes both real and synthetic records. Real

data of the Efpalio earthquake are broad-band (unfiltered) instrumentally corrected velocity records, re-sampled to 0.03 s as used in our previous calculations of the centroid moment tensor. The whole traces of the vertical component (containing weak P-, and strong S- and Lg-waves) are used, without any phase pre-selection. In the synthetic tests, we use the same source-station configuration as in the real case, and the source is situated under the coordinate origin at a depth of 9 km. Synthetics are calculated by the discrete-wavenumber method (code AXITRA of Coutant, 1989, based on Bouchon, 1981 and Kennett and Kerry, 1979). The double-couple focal mechanism from Sokos et al. (2012) is used (Table 1), but synthetic tests consider also two other mechanisms described later. The
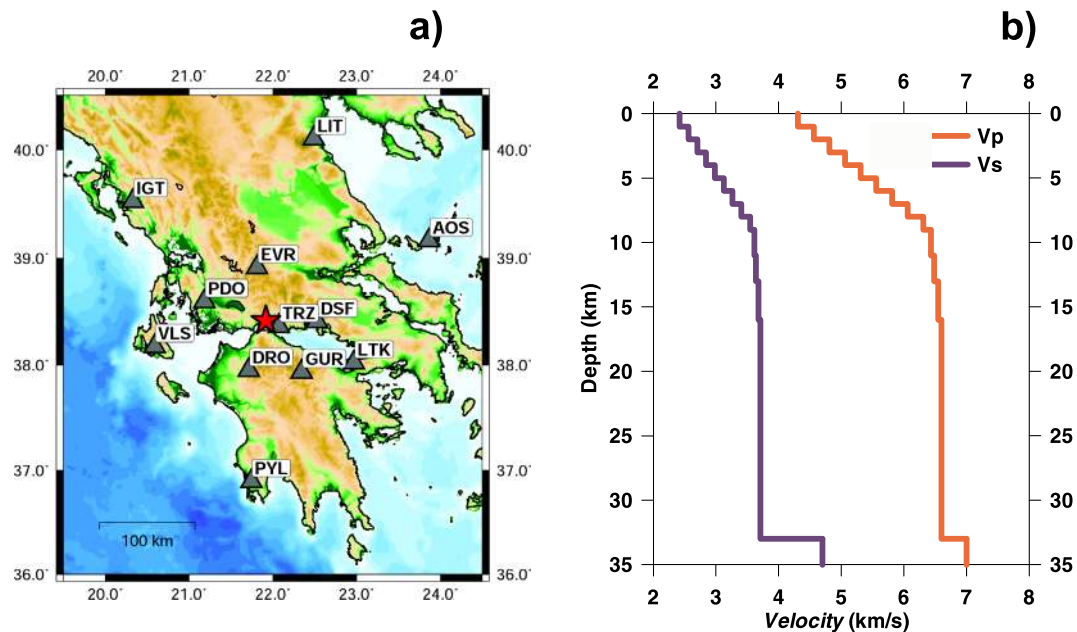

Fig. 1 Event 1, Efpalio 2010 earthquake. **a** Source-station configuration. **b** Velocity model. They apply both to synthetic tests and real-data calculations

location of synthetic data is performed with the same velocity model as used in the forward modeling. The synthetic data are noise free. Nevertheless, the synthetic tests are meaningful because SSA represents an approximate method, not necessarily returning correct hypocenters. The grid search is made with horizontal steps of 1 km, while the depth step varies in the applications from 3 to 5 km.

3 Synthetic tests

The source-station configuration and the velocity model are those of Fig. 1, simulating the Efpalio earthquake. The model event has its epicenter at $x=0$, $y=0$. The picker window width is 1 s.

Test A This test has two objectives: (i) To compare use of the RPA/LPA and STA/LTA picker and (ii) to evaluate the effect of focal mechanism (Figs. 2 and 3). Three focal mechanisms are considered: normal (characterized by the strike/dip/rake angles=102°/55°/–83°), reverse (102°/55°/83°), and strike-slip (102°/89°/1°). We analyze results from the space-time dependent brightness (Eq. 5). For both pickers and all three mechanisms, the method provided correct position and origin time of the source, but the properties of the brightness field were different. Here in Fig. 2, we concentrate on the x–y brightness maps at the origin time (i.e., we present a single snapshot $B_m(ot_{opt})$ for each tested case). Using RPA/LPA, the maximum brightness values for the three focal mechanisms—normal, reverse, and strike-slip— are 0.58, 0.65, and 0.78, respectively. Using STA/LTA, the values are 0.83, 0.93, and 0.97. Recall that the ideal value is 1. The result clearly demonstrates that the focal mechanism and the type of picker as well are affecting the results. For both pickers, the method works least efficiently in case of the normal mechanism. As for the picker itself, the maximum brightness values for STA/LTA are systematically higher than for RPA/LPA. However, as clearly seen from Fig. 2, the RPA/LPA brightness map is considerably sharper than STA/LTA. These effects are easily understandable when comparing the picker traces shifted according to the optimum source position (Fig. 3). Strength of the P-wave varies across the network due to the radiation pattern and distance; therefore, the pickers do not always attend their maxima (=1) at the P-wave arrival. When the picker is not maximized at the P-wave group at some station, this station weakly

contributes to the stack. For example, in case of normal mechanism and the RPA/LPA picker, the P-arrival is well tracked at only 7 from the 12 stations (thus we obtained brightness 0.58=7/12); even at the nearest station, the first arrival is missed by the RPA/LPA picker. On the other hand, the STA/LTA picker correctly tracks P arrivals at 10 from 12 stations even for the normal mechanism (brightness=0.83). Although STA/LTA is better in this sense, its disadvantage is that it gets many maxima of the picker trace with almost unit amplitude. That is why, using STA/LTA, various phases are apparently stacked "well", and consequently, the brightness map is blurred (Remark: Grigoli et al. (2014) overcome this problem by combining both P and S brightness.). To summarize, based on the test, we found sharper brightness maps for the RPA/LPA picker and a progressively better performance of the method from the normal towards reverse and strike slip mechanism.

Test B This test demonstrates how to monitor the effect of the source depth (Fig. 4). In Fig. 4, we plot the optimum brightness value attained across the spatial source grid as a function of the trial origin time: $B_{opt}(ot_i) = \max_m (S_m(t = ot_i))$. The 0.3 s advance of the optimum origin time with respect to its true value (shown as 30 s in Fig. 4) is due to a small numerical ringing before the first arrival, same in all stations. The example is for the RPA/LPA picker and the three focal mechanisms. The trial depths at which the brightness maximizes are indicated by labels. It can be seen that close to the optimum origin time, the possible source depths are 6 or 9 km, with almost no preference of the correct (prescribed) value of 9 km. Poor resolution of the depth is not surprising when using only P-waves. That is why, in all the paper, we concentrate mainly on the epicenter location.

4 Real data—Efpalio earthquake

The method is applied to real recordings of the Efpalio earthquake at 12 stations of Fig. 1 (event 1 in Tables 1 and 2). The picker window width is 1 s. Figure 5a represents the map view of the space-time dependent brightness maps; the three selected snapshots refer to three values of the trial origin time (0.4 s before, at, and 0.4 s after the optimum value OTopt). The two pickers, RPA/LPA and STA/LTA, are compared (for the
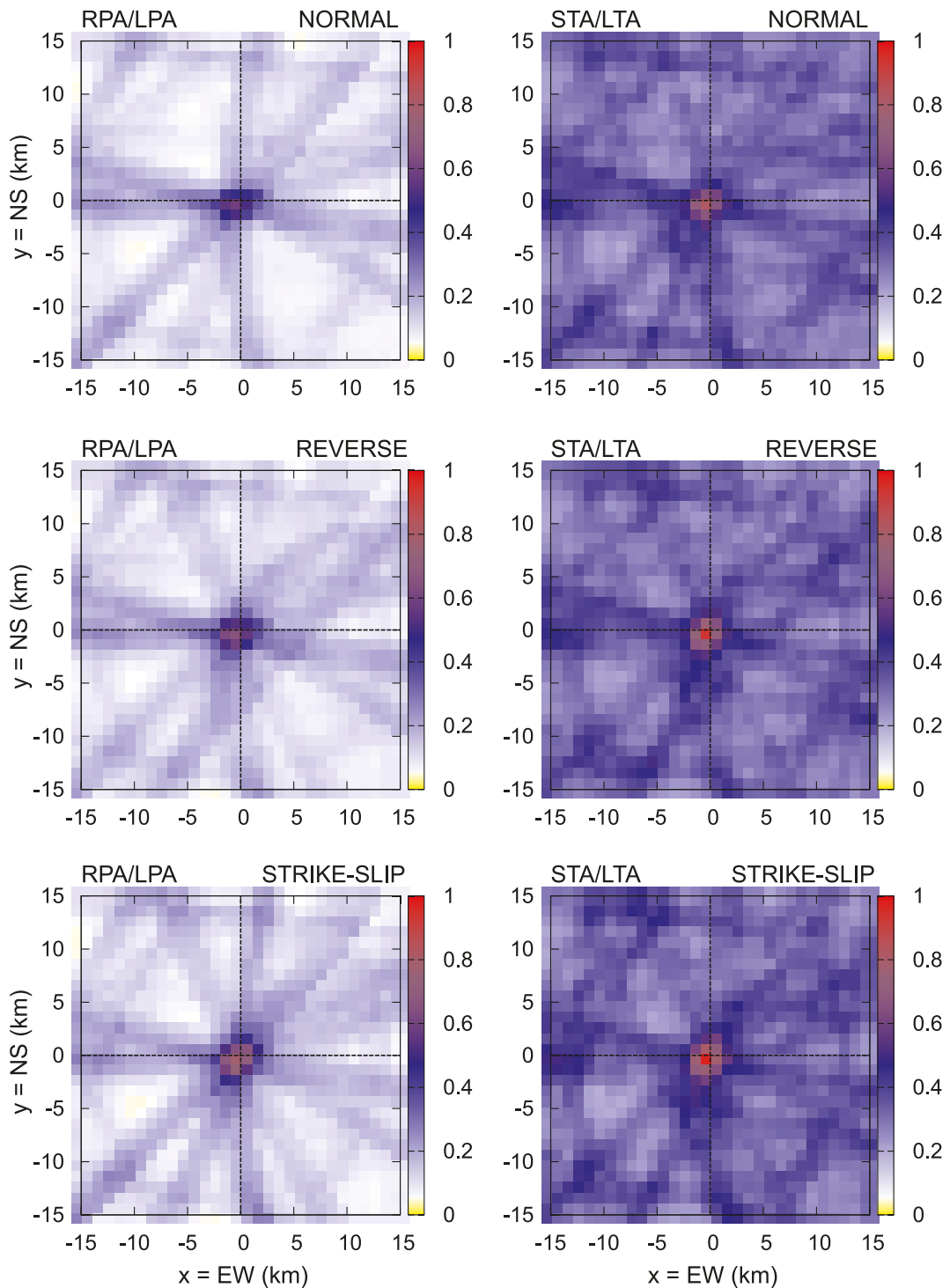
Fig. 2 Synthetic test A. Brightness maps at origin time are compared to study effects of the picker (left RPA/LPA, right STA/LTA) and focal mechanism (top=normal, middle=reverse, bottom=strike-slip). Correct position of the epicenter is in the middle of the plot

animation showing the whole temporal variation of the RPA/LPA brightness map with trial origin time, see

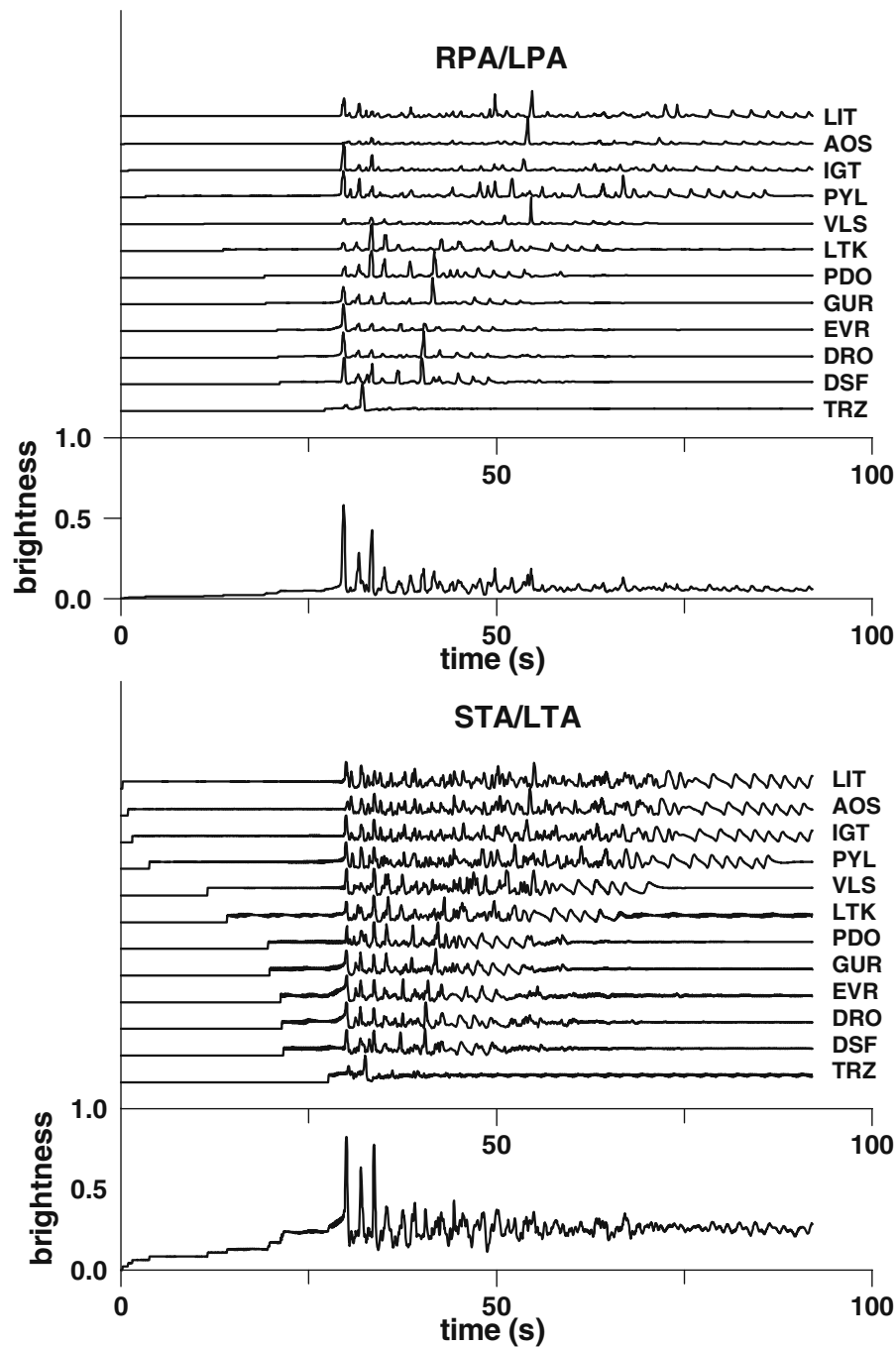Supplement S1.) The results are presented for the formally best value of the depth of 15 km, but (as in

Fig. 3 Synthetic test A. Comparison of the picker traces (*top* RPA/LPA, *bottom* STA/LTA) for normal focal mechanism. The traces are shifted according to the optimum source position. Their stack is plotted at the bottom. The origin of time axis (t=0) is formally shifted 30 s before the true origin time of the synthetic event

synthetic test B) the depth resolution was poor, with no strong preference between the depths 6, 9, and 15 km, as documented in Fig. 5d. Although the peak values of the brightness are lower for RPA/LPA (0.55) than for STA/LTA (0.75), similarly as in synthetic test A the RPA/LPA picker provides a sharper brightness pattern, hence preferable. The earthquake has a normal mechanism; therefore, as explained in synthetic tests, it poses a relatively low value of the optimal RPA/LPA brightness; 0.55 means that in fact only 6–7 stations constrained the
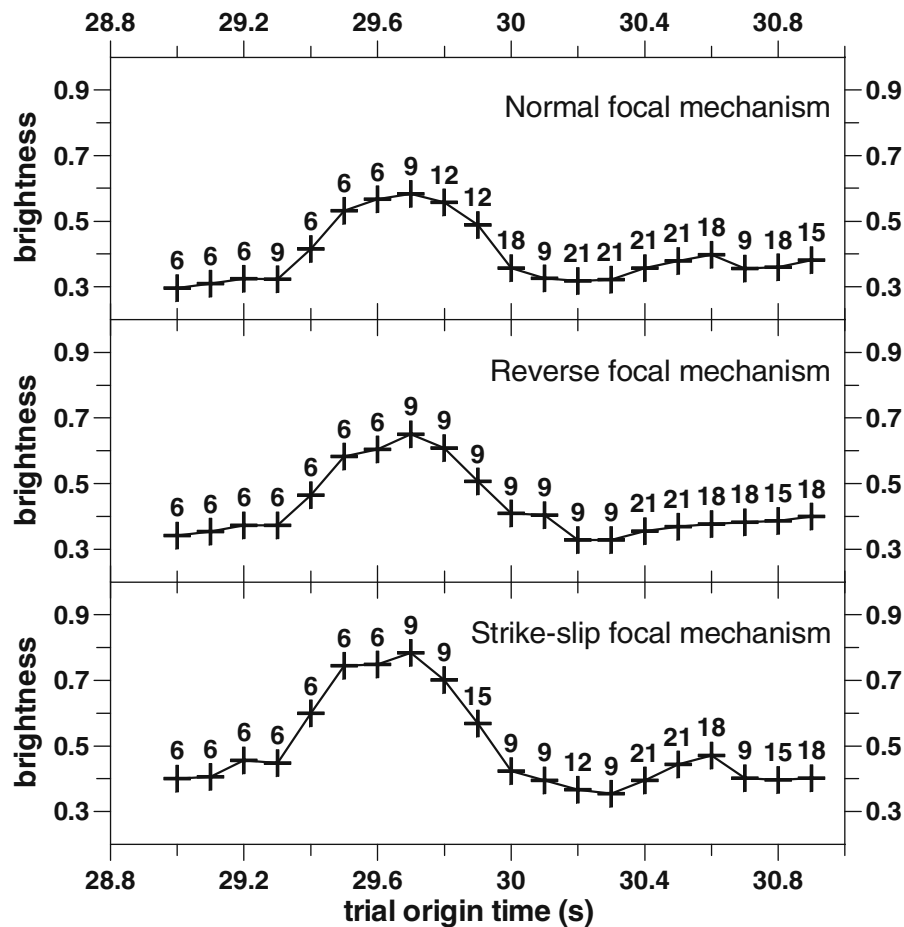
Fig. 4 Synthetic test B. Variation of the RPA/LPA brightness with trial origin time for three focal mechanisms (*top* normal, *middle* reverse, *bottom* strike-slip). Each value represents the maximum brightness across the spatial source grid. The corresponding source depth is marked by labels. The origin of time axis (t=0) is formally shifted 30 s before the true origin time of the synthetic event

location. Another factor, contributing to the relatively low brightness, is the limited knowledge of the true velocity model. In preliminary experiments, the seismograms were systematically poorly stacked at epicentral distances greater than ~100 km where the first arrivals are due to Pn waves. Then, we varied P velocity below Moho and found that using 7 km/s (as in Rigo et al., 1996) considerably improves the trace alignment, even at the two most distant stations; see Fig. 5c (left). The obtained RPA/LPA solution (x=0, y=1, see Table 2) is very close to the epicenter calculated by Sokos et al. (2012); shown in Fig. 5a as x=0, y=0.

Finally, as an example of a faster calculation, Fig. 5b presents also the space-dependent brightness (Eq. 4), without seeking origin time. We remind the reader that in this case, each trial source (i.e., each point of the map) has its individual optimum time at which the stack of picker traces is maximized. The maximum brightness is

a bit higher than in the space-time dependent approach, but the pattern of the station strips is lost (smeared).

5 Real data—three more earthquakes

In this section, we use the SSA method based on the RPA/LPA picker for three more earthquakes covering a broad range of magnitudes, source depths, epicentral distances, and focal mechanisms. Table 1 gives the earthquake parameters from previous studies, and the published epicenter is plotted in subsequent figures at x=0, y=0. Table 2 is the SSA location of this paper, including the computational parameters (e.g., the velocity models, the window widths); the results are expressed by means of increments with respect to the solutions of Table 1. These increments should not be misinterpreted as an estimate of the location error.
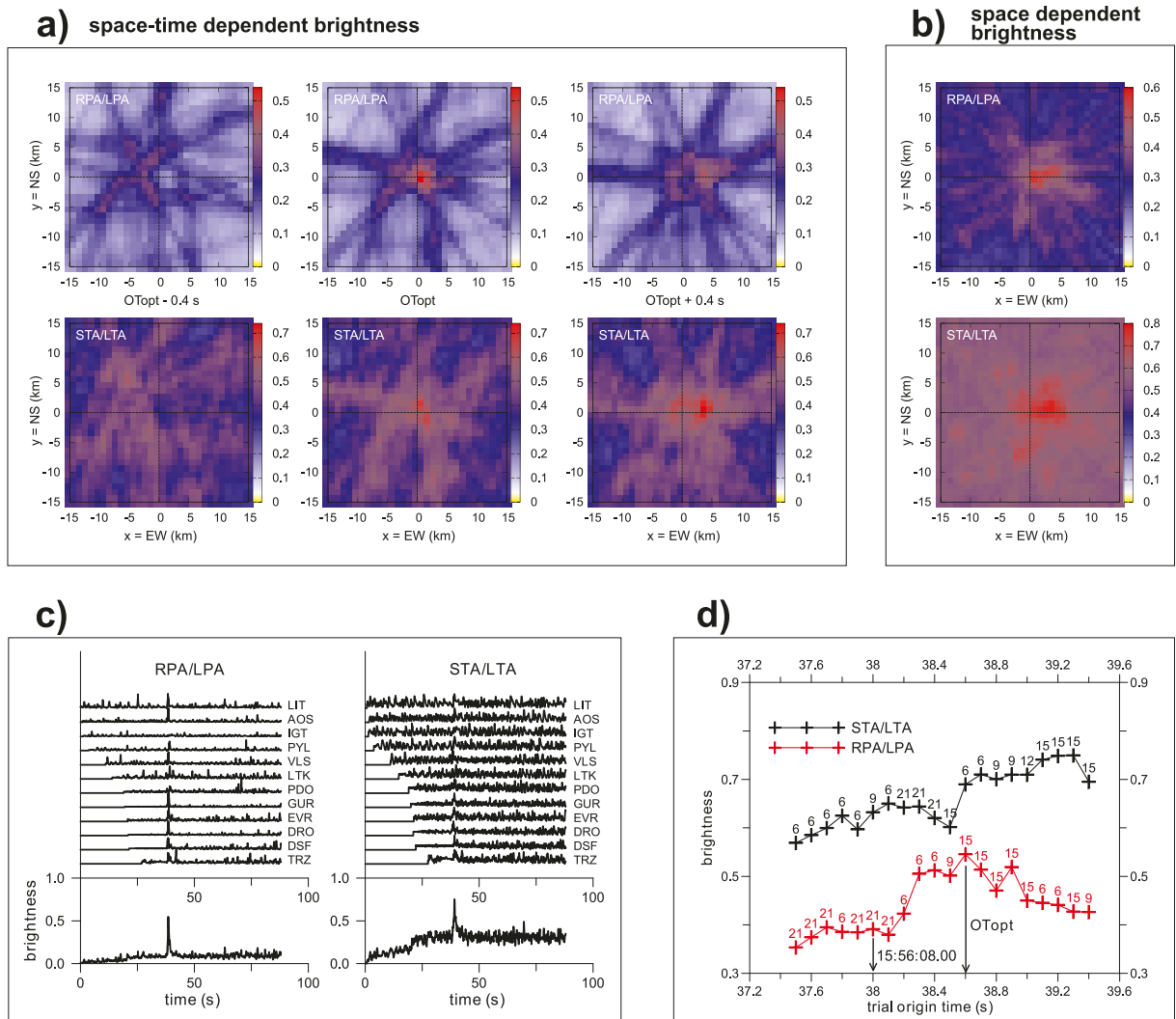
Fig. 5 Real data, Event 1. **a** Map view of the space-time dependent brightness according to Eq. (5); the three snapshots correspond to three values of the trial origin time (the *left*, *middle*, and *right* plots refer to 0.4 s before, at and 0.4 s after the optimum origin-time OTopt, respectively). Compared is the performance of two pickers, (*top* RPA/LPA, *bottom* STA/LTA). **b** The brightness map calculated according to Eq. (4), without seeking the origin time (*top* RPA/LPA, *bottom* STA/LTA). **c** Picker traces shifted according to the optimum source position (*left* RPA/LPA, *right* STA/LTA). **d** Variation of the maximum brightness with trial origin time; the corresponding source depth is marked by labels. The origin ($t=0$) of time axes in panels **c** and **d** is 38 s before the published origin time 15:56:08.00 UTC (Table 1)

Animations of the space-time brightness (i.e., snapshots for a variable trial origin time) are in Supplements S2, S3, and S4.

Event 2 Event 2 is the 2012 Mw 3.8 strike-slip event of a ~20 km source depth (Tables 1 and 2, Fig. 6). The earthquake occurred in the region activated in 2008 by the Mw 6.3 Andravida (Movri Mountain) earthquake; see, for example, Gallovič et al. (2008). We used instrumentally corrected broad-band velocities (re-sampled at

0.03 s, again because the same sampling was used in our centroid moment calculation). Six stations, covering epicentral distances from 58 to 94 km, have a good azimuthal coverage. The brightness map-view pattern in Fig. 6b is clear, making evident the contribution of the individual stations. All station "strips" cross each other at the epicenter, except KFL; the KFL "strip" is marked in the middle panel of Fig. 6b. The poor alignment of station KFL is explained by its complex picker trace (Fig. 6c). The location would not change if we remove
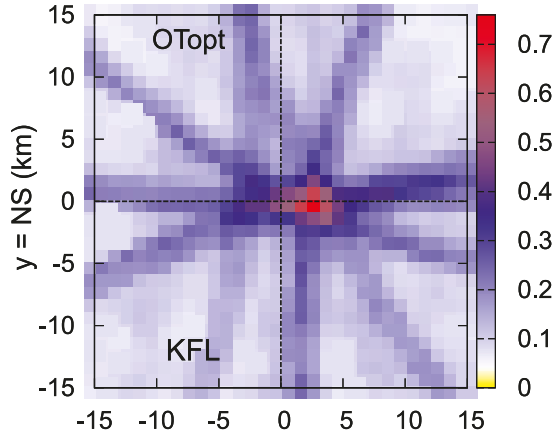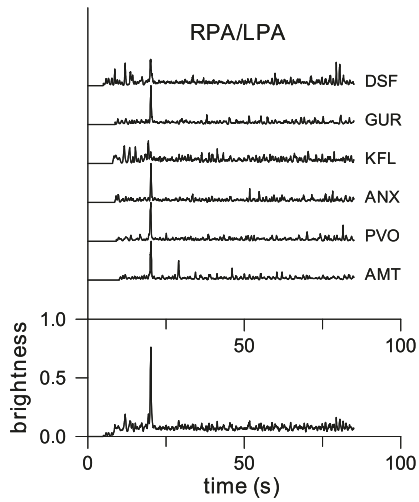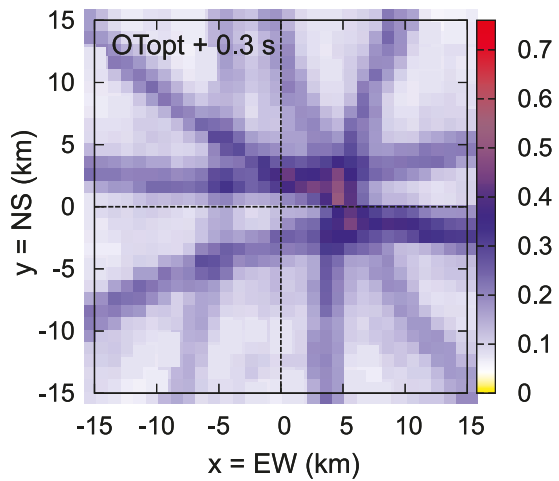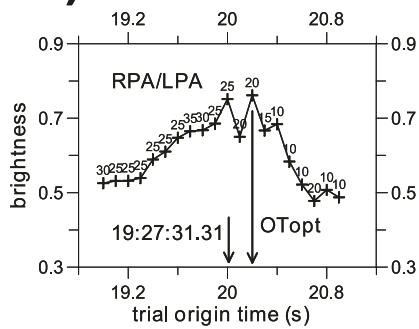
a)
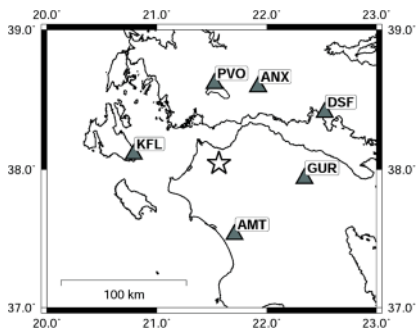
b)
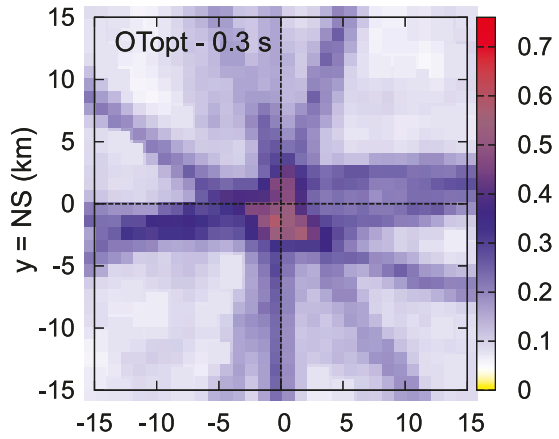
c)

d)

◀ **Fig. 6** Real data, event 2. **a** The source-station configuration. **b** Selected snapshots of the space-time brightness, calculated with the RPA/LPA picker. The optimum solution (Table 2) is in the middle panel. The strip corresponding to KFL station is marked in the same panel. The *top* and *bottom* panels correspond to the trial origin time of 0.3 s before and 0.3 s after the optimum origin time OTopt. The previously published location (Table 1) is in the center of each panel. **c** The RPA/LPA picker traces shifted according to the optimum source position. **d** Variation of the brightness with trial origin time; the corresponding source depth is marked by labels. The origin (*t*=0) of time axes in panels **c** and **d** is 20 s before the published origin time 19:27:31.31 UTC (Table 1)

KFL. The SSA location is within 3 km from the previously determined catalog hypocenter. If we setup the allowed brightness threshold to be, for example, at 0.65, corresponding to 85 % of the optimum brightness (red color in Fig. 6b), the epicenter relative uncertainty would be ~±2 km, but the depth resolution is poor, 10–35 km (Fig. 6d).

Event 3 Event 3 is the Mw 6.3 L'Aquila, Central Italy 2009 earthquake, a normal-faulting event, located in this paper with 9 stations (Tables 1 and 2, Fig. 7). This example represents the case where we started the SSA location with 17 stations (up to 102 km), but finally, we used only 9 stations with epicentral distances ranging from 2 to 48 km, since all others blurred the image. Fig. 7b shows the snapshots together with a possible model of the fault plane (Gallovič and Zahradník, 2012; Ameri et al., 2012). The SSA epicenter location is in agreement (within the 1-km grid step) with the previously published solution. Nevertheless, the brightness spot indicates a possible small shift of the true epicenter westward. Apparent movement of the bright spot with varying trial origin time, resembling "rupture propagation" in Fig. 7b, is an artifact. It was present also in synthetic tests for this event, using a point source embedded in layered 1D models (not shown here), having nothing to do with the rupture propagation over the fault.

Event 4 Event 4 is the Mw 7.2 Van, Eastern Turkey 2011 earthquake (Tables 1 and 2, Fig. 8). This is a reverse-faulting event located in this paper by means of relatively distant strong-motion accelerographic stations. Initial attempts to use seven accelerographs up to 220 km indicated insufficiently sharp picker traces at some stations. Finally, the SSA method has been applied using 4 stations in epicentral distances ranging from 42

to 160 km. As seen from Fig. 8b, the stations constrain the epicenter well. The SSA location is relatively far from the reference solution, e.g., 4 km in the EW direction and 12 km in depth (compare Tables 2 and 1, respectively). However, the present SSA location from P-waves is very close to the re-location from P and S waves described in Table 2 and Figs. 2 and 3 of Gallovič et al. (2013); their solution was at Lat 38.716 (°N), Lon 43.405 (°E), and depth 8 km, which means that the increments of the SSA with respect to that solution are just 0 km, 1.3 km, and −1 km in the NS, EW, and depth direction, respectively. Figure 8b displays the SSA solution together with the fault plane used in our multiple-source modeling (Zahradník and Sokos, 2014; Gallovič et al., 2013). Although two-three main slip patches were found in the referenced papers, our SSA location does not indicate their individual nucleation points (multiple hypocenters). On the contrary, Evangelidis and Kao (2014) were able to resolve two high-frequency sources with their SSA back-projection method, it is because they assumed the hypocenter to be a priori known.

6 Real data—discussion

All together, the tested real cases show that the SSA method is a robust tool, competitive with the classical location techniques based on arrival-time readings.

It works with full waveforms without any prior identification of the P-wave group and the arrival time. The new RPA/LPA picker of this paper makes the brightness maps very clear. Besides the formally best source position, the method automatically provides also the relative uncertainty estimate (measured by a finite size of the bright spot). The uncertainty is due to combined effect of the unclear first arrivals (due to noise and radiation pattern), source-station configuration, and imprecise velocity model. The brightness maps may indicate a need to remove those stations which blur the brightness pattern due to improper velocity model along certain paths (as we did for event 3). They may also guide us how to revise velocity models (as we noted when processing event 1). Equally well, the maps may also inform us that more stations should be added to better constrain the solution. With using only P-waves, the depth resolution is naturally limited. Possible implementation of S-waves aimed at improving the depth resolution will be studied elsewhere. The method of Grigoli et al. (2014) seems
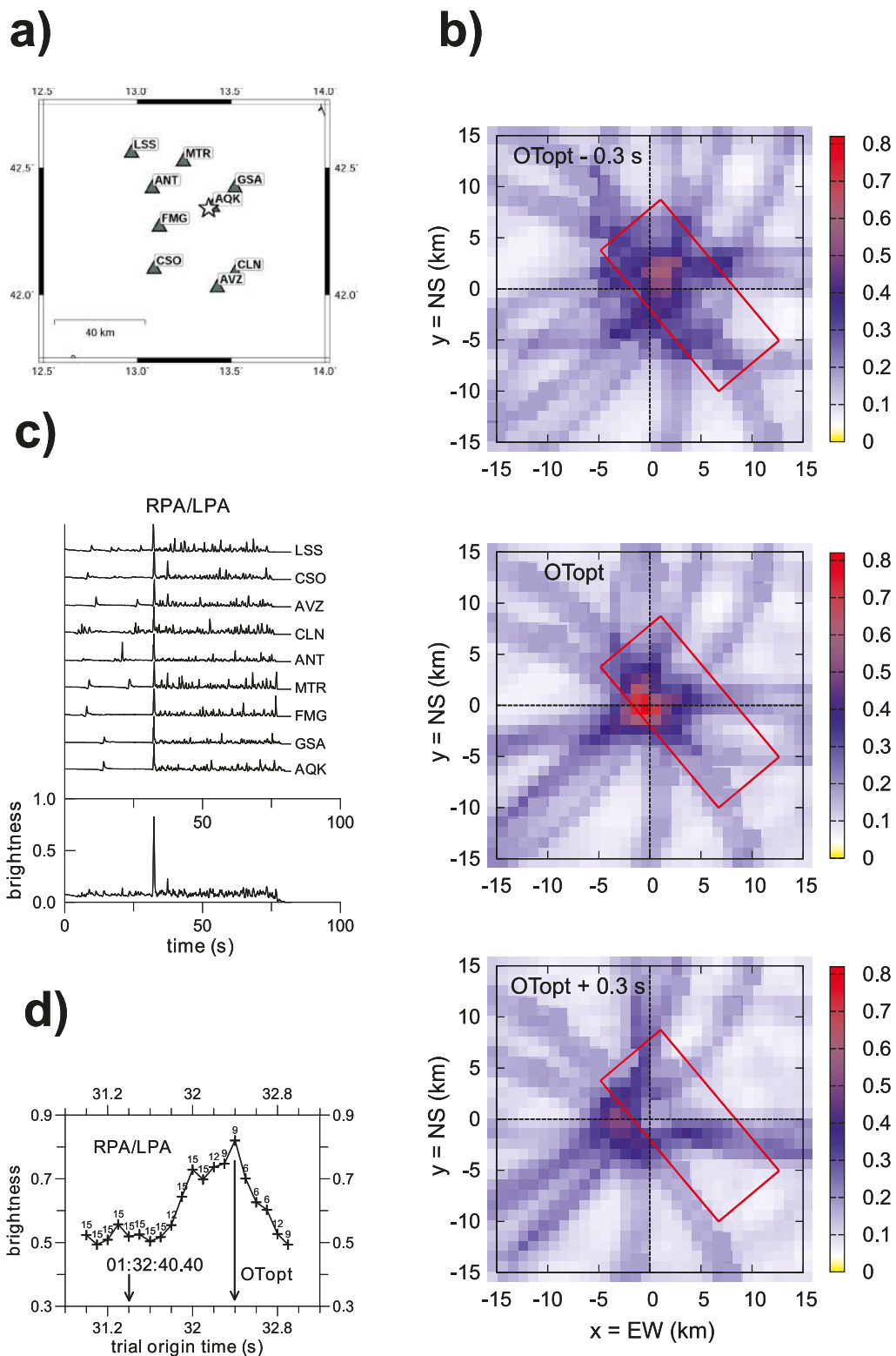
Fig. 7 Real data, event 3. The layout is the same as in Fig. 6. The origin (*t*=0) of time axes in panels **c** and **d** is 31.4 s before the published origin time 01:32:40.40 UTC (Table 1). *Red rectangle* in panel **b** shows the fault plane after Gallovič and Zahradník, 2012
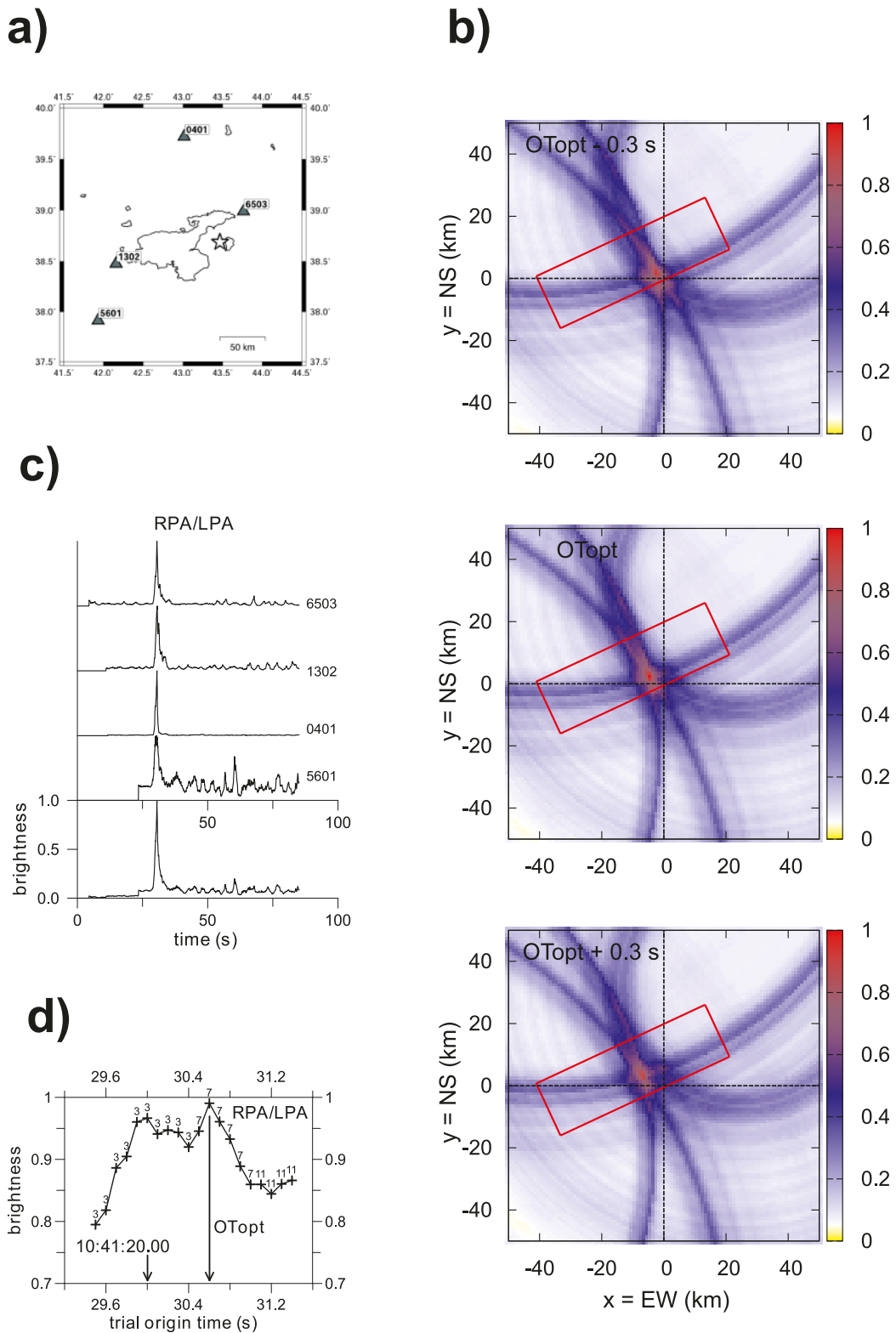
Fig. 8 Real data, event 4. The layout is the same as in Fig. 6. The origin (*t*=0) of time axes in panels **c** and **d** is 30 s before the published origin time 10:41:20.00 UTC (Table 1). *Red rectangle* in the panel **b** shows the fault plane after Gallovič et al., 2013

useful, at least when the arrival of S-waves is not in the P-wave coda.

The uncertainty issue, already mentioned several times above, still needs a more discussion. Let us start with demonstrating effects of the RPA/LPA picker window width. To this goal, we return to the most thoroughly studied earthquake of this paper—event 1. Figure 9 shows the brightness map for four picker widths: 2, 1, 0.5, and 0.25 s. The 2-s width yields a large brightness, but the spatial resolution is very low (the maximum-brightness spot is large). When the window width decreases to 1 s, the spatial resolution improves. When further decreasing the picker width to 0.5 s, the maximum brightness considerably decreases due to increasing complexity of the picker traces and their decreasing coherence. Although the solution is still resolved correctly close to $x=0$ and $y=0$, many other spots with similar brightness appear on the map and make the location highly non-unique. The width of 0.25 s causes a total loss of correlation. A similar empirical approach was used for all four events of this paper, trying to avoid the extremely low resolution (a too large width of the picker) as well as the lost of coherence (a too small width). However, no optimization was made in terms of the picker width, temporal sampling of waveforms, or the studied frequency band. All records (velocity, dominant frequencies ~0.2–2.0 Hz) were processed up to their Nyquist frequency. The picker window width of 1 s was found applicable to all near-regional records of this paper, except event 4. In case of event 4, the emergent first arrivals of velocity were not picked well; thus, acceleration was used instead, but complexity of the picker traces called for smoothing by a 3-s window width. Tests to employ causal band-pass filtering are underway to possibly improve the picker quality and frequency band, similarly to, e.g., the use of kurtograms by Langet et al. (2014).

As demonstrated by Fig. 9, the picker window width controls the width of the individual station strips, whose crossing consequently produces the bright spots. The
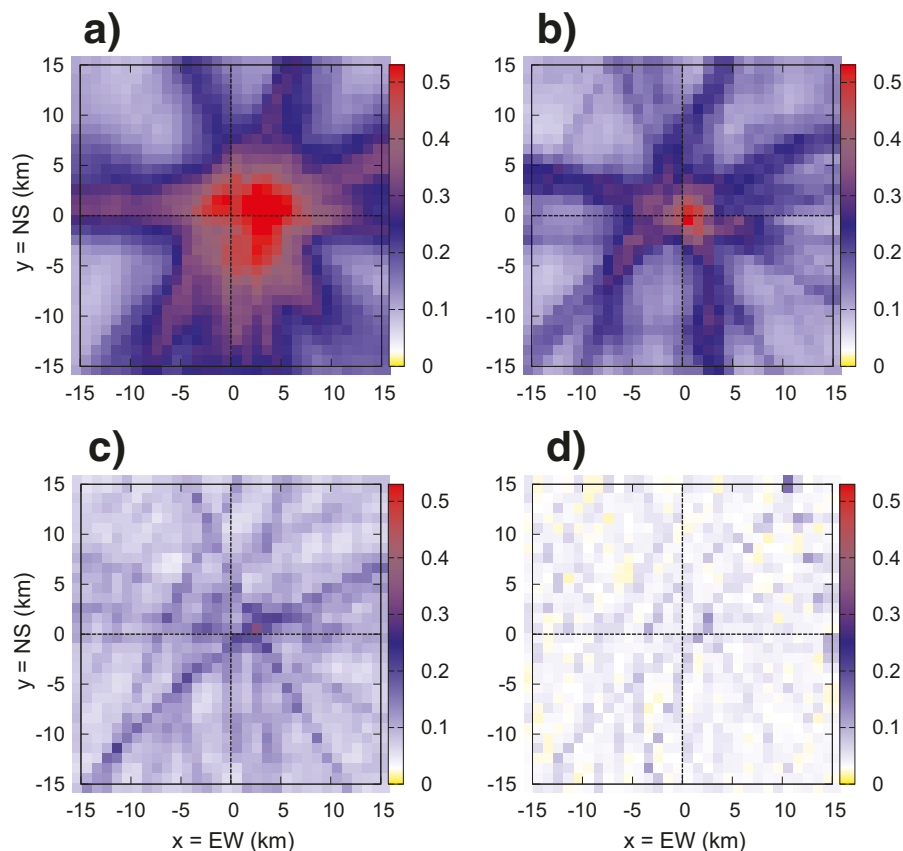

Fig. 9 Effects of the picker window width. Shown is the brightness map at an optimum origin time for four picker widths: **a** 2 s, **b** 1 s, **c** 0.5 s, and **d** 0.25 s. The example refers to event 1

bright-spot size (at a chosen brightness value) is a measure of the location uncertainty, but Fig. 9 well explains that the uncertainty estimate is only relative. Indeed, it depends on the picker width; see the large and small size of the red spot in panels a) and b) in Fig. 9, respectively. To get a formal, quantitative estimate of the location uncertainty, the picker width should be proportional to the travel-time data error (errors of the picking and velocity model). This is explained in the next section, where the width of station strips is directly related to the assumed data error. Any estimate of data error is always difficult (Zahradník and Custódio, 2012). Figure 9 shows that although we do not know the true value of the data error in a real case, we can say something about its lower bound. Indeed, the data error is at least +/− 0.25 s (equivalent to the picker width of 0.5 s), because with a narrower window width the picker traces become incoherent. In simpler words, due to imprecise velocity model, the narrower station strips have no joint intersection. Therefore, real earthquake locations by SSA, inherently including imprecise velocity models, always need some minimum amount of the assumed data error, and they consequently provide the lower bound of the location uncertainty.

7 Modeling the brightness field—a tool for analyzing location capability of a seismic network

In this section, we provide a theoretical model of the brightness maps. It is proven that stations contribute to the maps by individual strips whose width is controlled by an assumed data error. We also explain that models of the brightness maps can be used to investigate location capability of seismic networks.

Assume a true source position X^* (a three-component vector) and origin time H^*. Further assume a velocity model, so that travel times can be calculated from any source position to any station. The travel time $TP(X^*, S)$ from the true source X^* to station S is to be fitted by grid searching trial space positions X_m (m=1,2,…M) and trial origin times H_i (i=1,2,…I). For any station S, we construct a function

$$F(X_m, H_i, S) = TP(X_m, S) + H_i - TP(X^*, S) - H^* \quad (6)$$

If the medium is 1D, then the map view of $F(X_m, H_i, S)=0$ is a circle centered at station S, passing through the true source at X^* in time H^*. If $H_i < H^*$ or $H_i > H^*$, the true source is within or outside the circle, respectively. The method can also work with any (3D) model, with the only difference that then the curves are no more circular. Taking into account the station-dependent travel time errors (−ERR(S), +ERR(S)), we consider time residuals FF(S)=|$F(X_m, H_i, S)$|−ERR(S). The points for which FF(S)<0 form a strip, substituting the circle of station S; the width of the strip is proportional to ERR. For simplicity, hereafter, we assume ERR independent of S. The true source position is close to the trial point at which the inequality FF(S)<0 holds for most of the stations. Therefore, instead of mapping the time-residual values FF, we introduce and map an objective function NOS(X_m); the NOS(X_m) equals to the number of stations S for which FF(S)< 0 holds at a given trial source point X_m and trial origin time H_i. In this way, the NOS map is analogous to the brightness map using station network, being most intensive at places where the most station strips cross with each other.

The method is demonstrated in Fig. 10, using ERR= 0.3 s. Shown are three snapshots of the brightness whose trial origin time is smaller, approximately equal, and larger than the true origin time. Each snapshot shows four strips related to four stations. The figure compares the theoretical and real brightness maps for event 1, using picker width of 1 s.

This theoretical model is a simple tool helping to understand what happens when processing data in a certain network. For example, if in real data case some station strip is missing or dispersed (for example, the strip of station TRZ in Fig. 10, or KFL in Fig. 6), it means that the picker was not effective at that station, or the velocity model is not appropriate, or the station has some instrumental problem. In cases like that, the station cannot contribute to the stack and to the location. The finite size of the intersection of the station strips informs about the location uncertainty. Note that it depends on the width of the strips, controlled by the choice of ERR. It is equivalent to the choice of the picker window widths in real brightness maps. Until not being determined by the true travel time errors (due to picking and imprecise velocity model), the uncertainty estimate is only relative.

Importantly, this simple tool is applicable also without any real (measured) arrival time. In such a case, we simply *assume* a given source position and origin time, calculate arrival times $TP(X^*,S)+H^*$ for all stations, and try to fit them by the spatiotemporal grid search over X_m and H_i. Naturally, a value of ERR needs to be also

Fig. 10 Modeling the brightness field. Shown are three snapshots of the brightness *x–y* (Lon-Lat) map whose trial origin time is smaller (*top*), approximately equal (*middle*), and larger (*bottom*) than the true origin time; the temporal difference between the snapshots is 0.2 s. Each snapshot shows four strips related to four stations (*inset*). Left—theoretical strips, right—strips for real data case, event 1, RPA/LPA
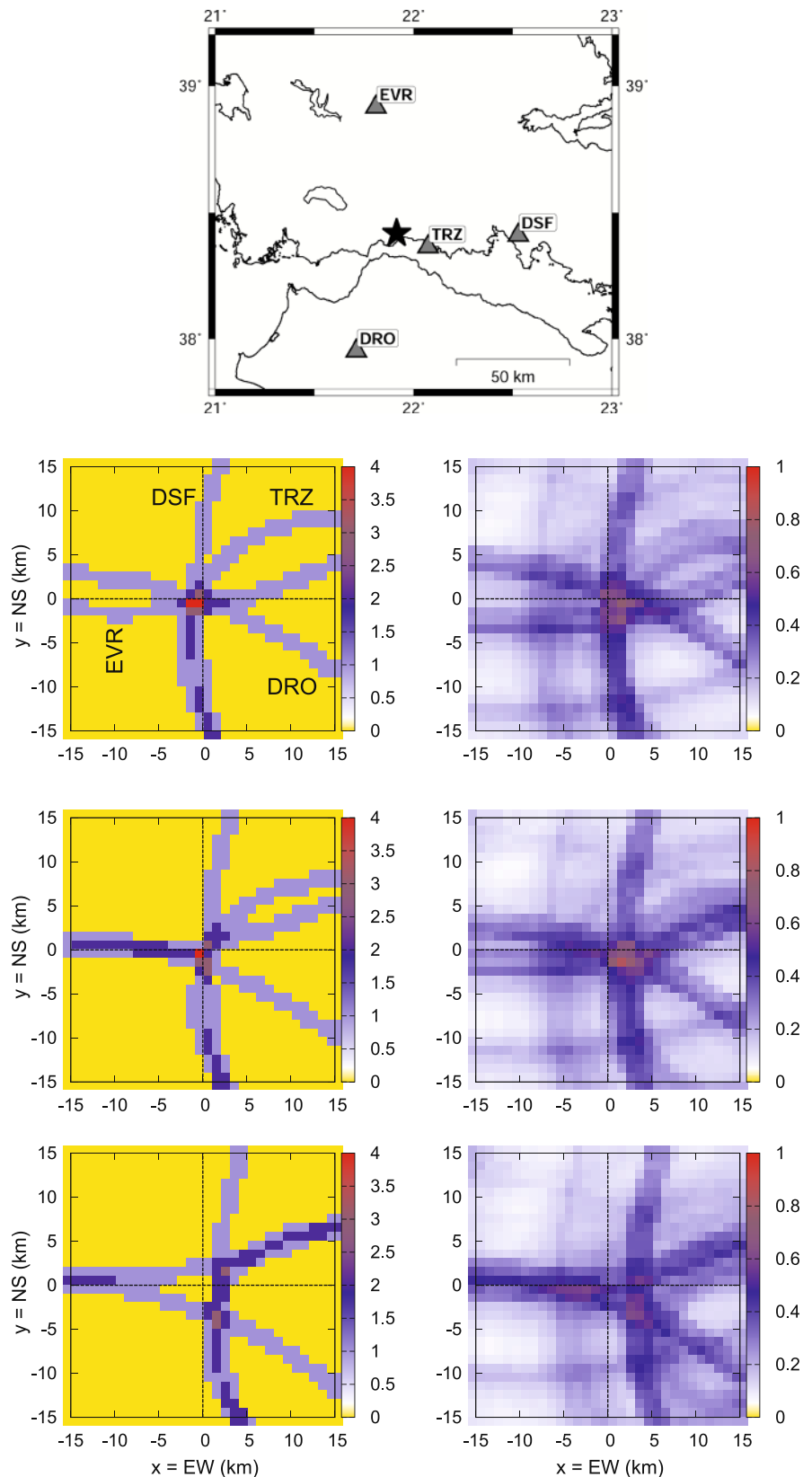
assumed. In this sense, the method demonstrates the location capability of the considered stations, and, as such, it is applicable in designing seismic networks or upgrading them. It is better than the standard analysis of the location capability based on error ellipsoids (singular vectors and values of the linearized location problem), because it fully takes into account the intrinsic non-linearity of the location problem. Moreover, different velocity models can be used in the forward and inverse part of this method, i.e., to calculate in Eq. (6) the terms $TP(X^*, S)$ and $TP(X_m, S)$, respectively, thus also helping to understand effects of the limited structural knowledge.

The method has been used to quantify the location uncertainty in the Little Carpathians (Slovakia) seismic network (Fojtíková et al. 2013).

8 Conclusion

We analyzed the location of earthquakes using seismic records without picking and extracting arrival times. The basic idea of the method goes back to the source scanning algorithm (SSA) of Kao and Shan (2004), in which records in a seismic networks are repeatedly stacked for a set of pre-defined trial source points, and the hypocenter is identified with the point providing the best stack (the largest brightness). We focus on P-waves in near-regional networks. As such, the P-wave groups are strongly varying from station to station due to focal mechanism and structural effects; hence, stacking them without prior pre-processing of the P-wave group is not viable. Therefore, following Grigoli et al. (2013), we first convert seismograms into (time varying) picker traces, and then stack the picker traces. Extending the idea of the picker, we compare the STA/LTA picker with a new one, called RPA/LPA, in which we measure ratio of the summed absolute values of the waveform in the right and left part of a moving time window. The latter is found preferable because it is more strongly highlighting the first arrival, hence providing less blurred brightness maps than those based on the STA/LTA picker. For more sophisticated approaches see, for example, the first arrival enhancement by kurtosis (Langet et al., 2014).

Nevertheless, the method is not free of limitations. As in any (absolute) location approach, we need a good velocity model. Moreover, the performance of the method is somewhat dependent on focal mechanism; we have shown that quality of the stack may improve from

normal, to reverse and strike-slip events. The space dependent brightness (Eq. 4) is fast, but does not implicitly provide the origin time. The space-time-dependent brightness (Eq. 5) provides both the hypocenter and origin time. Moreover, it better reveals the effect of the individual stations upon the solution (via station strips). Naturally, as in any location based exclusively on P-waves, there is a poor resolution of the source depth. Varying the trial origin time in the SSA method, we can directly observe its tradeoff with source position. This effect has to be carefully distinguished from potential effects of the rupture propagation which were not studied/revealed in the present paper; they would require an independent, precise knowledge of the hypocenter and very accurate crustal models. For example, Evangelidis and Kao (2014) made use of specific station corrections, based on waveform cross-correlation that fixed the SSA calculation to a known hypocenter.

Although the method always identifies some "optimum" trial source point, characterized by the largest brightness value, equally valuable is the complete brightness map, because it clearly identifies location problems. Simply speaking, highly blurred images, or images with several bright spots of a comparable strength might signalize problems. It is relatively easy to identify the main reasons of the blurring, for example to find out that P-waves at some stations cannot be aligned with the others. There is a variety of reasons for such a misalignment (e.g., use of improper velocity model, local site effects, instrumental disturbances, etc.). Inspection of the brightness maps can help to eliminate the most problematic stations. The final brightness maps for the optimized origin time have a bright spot of a finite size which can be used to quantify the location uncertainty. The uncertainty estimate remains only relative until we can setup the pulse widths in the picker traces proportional to the expected data uncertainty (due to the picking error and the velocity model error).

The paper also provides a simple theoretical model of the brightness space-time field. The model is equivalent to a synthetic test of the grid search location. We assume a given source position and origin time, and make forward simulation of arrival times at stations. The arrival times are then fitted by grid searching the source position and origin time. However, opposed to standard approaches making use of the global time residual, our innovation consists in *counting stations whose arrival time is fitted within an assumed error limit*; see

NOS(X_m) in the preceding section. Plot of this objective function is fully equivalent to the space-time brightness maps; each station contributes by (a temporarily evolving) strip, and the maximum overlap of the station strips is the brightness spot. The spot (of a finite size), is a measure of the location uncertainty. This measure fully takes into account non-linearity of the location (similarly to the NonLinLoc code of Lomax et al., 2000), hence is preferable over standard error ellipsoids of the linearized location. Most importantly, this uncertainty assessment needs only an assumed source position, station coordinates, and velocity model. It does not need any real (measured) arrival times; hence, this kind of the uncertainty estimate is applicable "without earthquakes" when designing or upgrading station networks.

For more applications of our SSA method published after submission of the present paper, see Quintero et al. (2014), Fojtíková and Zahradník (2014).

The Fortran computer codes developed for this paper are easy to use. Their implementation in ISOLA software (Sokos and Zahradník, 2008, 2013) is in preparation.

References

Ameri G, Gallovič F, Pacor F (2012) Complexity of the Mw 6.3 2009 L'Aquila (Central Italy) earthquake: 2. Broadband strong-motion modeling. J Geophys Res 117: no. B04308. doi:10.1029/2011JB008729

Bouchon M (1981) A simple method to calculate Green's functions for elastic layered media. Bull Seism Soc Am 71:959–971

Coutant O (1989) Programme de simulation numérique AXITRA. Res. Report LGIT, Grenoble, France

Evangelidis CP, Kao H (2014) High-frequency source imaging of the October 23, 2011 Van (Eastern Turkey) earthquake by back-projection of strong motion waveforms. Geophys J Int 196:1060–1072. doi:10.1093/gji/ggt437

Fojtíková L, Kristeková M, Málek J, Zahradník J, Progseis Ltd. (2013) Uncertainty in locations and moment tensors of micro-earthquakes in Little Carpathians improved by new

stations. 4th Annual Meeting of project AIM (Advanced Industrial Microseismic Monitoring). September, 11–14, 2013, Třešť castle, Czech Republic, http://www.ig.cas.cz/sites/default/files/Fojtikova_et_al_AIM2013.pdf (last accessed in November 2014)

Fojtíková L, Zahradník J (2014) A new strategy for weak events in sparse networks: the first-motion polarity solutions constrained by single-station waveform inversion. Seism Res Lett 85:1265–1274. doi:10.1785/0220140072

Gallovič F, Zahradník J (2012) Complexity of the M 6.3 2009 L'Aquila (central Italy) earthquake: 1. Multiple finite-extent source inversion. J Geophys Res 117: no. B04307. doi:10.1029/2011JB008709

Gallovič F, Zahradník J, Křížová D, Plicka V, Sokos E, Serpetsidaki A, Tselentis GA (2008) From earthquake centroid to spatial-temporal rupture evolution: Mw 6.3 Movri Mountain earthquake, June 8, Greece. Geophys Res Lett 36, L21310. doi:10.1029/2009GL040283

Gallovič F, Ameri G, Zahradník J, Janský J, Plicka V, Sokos E, Askan A, Pakzad M (2013) Fault process and broadband ground-motion simulations of the 23 October 2011 Van (eastern Turkey) earthquake. Bull Seism Soc Am 103:3164–3178. doi:10.1785/0120130044

Grigoli F, Cesca S, Vassallo M, Dahm T (2013) Automated seismic event location by travel-time stacking: an application to mining induced seismicity. Seism Res Lett 84:666–677. doi:10.1785/0220120191

Grigoli F, Cesca S, Amoroso O, Emolo A, Zollo A, Dahm T (2014) Automated seismic event location by waveform coherence analysis. Geophys J Int 196:1742–1753. doi:10.1093/gji/ggt477

Janský J, Novotný O, Plicka V, Zahradník J, Sokos E (2012) Earthquake location from P-arrivals only: problems and some solutions. Stud Geophys Geod 56:553–566. doi:10.1007/s11200-011-9036-2

Kao H, Shan SJ (2004) The source-scanning algorithm: mapping the distribution of seismic sources in time and space. Geophys J Int 157:589–594

Kao H, Shan SJ (2007) Rapid identification of earthquake rupture plane using source-scanning algorithm. Geophys J Int 168:1011–1020

Kao H, Shan SJ, Dragert H, Rogers G (2009) Northern Cascadia episodic tremor and slip: A decade of tremor observations from 1997 to 2007. J Geopys Res 114: B00A12. doi:10.1029/2008JBB006046

Kennett BLN, Kerry NJ (1979) Seismic waves in a stratified half space. Geophys J R Astron Soc 57:557–583. doi:10.1111/j.1365-246X.1979.tb06779.x

Langet N, Maggi A, Michelini A, Brenguier F (2014) Continuous kurtosis-based migration for seismic event detection and location, with application to Piton de la Fournaise volcano, La Réunion. Bull Seism Soc Am 104:229–246. doi:10.1785/0120130107

Latorre D, Virieux J, Monfret T, Monteiller V, Vanorio T, Got JL, Lyon-Caen H (2004) A new seismic tomography of Aigion area (Gulf of Corinth, Greece) from the 1991 data set. Geophys J Int 159:1013–1031

Liao Y, Kao H, Rosenberger A, Hsu S, Huang B (2012) Delineating complex spatiotemporal distribution of earthquake aftershocks: An improved source-scanning algorithm.

Geophys J Int 189:1753–1770. doi:10.1111/j.1365-246X.2012.05457.x

Lomax A, Virieux J, Volant P, Berge C (2000) Probabilistic earthquake location in 3D and layered models: introduction of a Metropolis-Gibbs method and comparison with linear locations. In: Thurber CH, Rabinowitz N (eds) Advances in seismic event location. Kluwer, Amsterdam, pp 101–134

Novotný O, Zahradník J, Tselentis GA (2001) Northwestern Turkey earthquakes and the structure inferred from surface waves observed in Western Greece. Bull Seism Soc Am 91:875–879

Quintero R, Zahradník J, Sokos E (2014) Near-regional CMT and multiple-point source solution of the September 5, 2012, Nicoya, Costa Rica Mw 7.6 (GCMT) earthquake. J South Am Earth Sci 55:155–165. doi:10.1016/j.jsames.2014.07.009

Rigo A, Lyon-Caen H, Armijo R, Deschamps A, Hatzfeld D, Makropoulos K, Papadimitriou P, Kassaras I (1996) A microseismic study in the western part of the Gulf of Corinth (Greece): implications for large scale normal faulting mechanisms. Geophys J Int 126:663–688

Sokos E, Zahradník J (2008) ISOLA a Fortran code and a Matlab GUI to perform multiple-point source inversion of seismic data. Compt Geosci 34:967–977. doi:10.1016/j.cageo.2007.07.005

Sokos E, Zahradník J (2013) Evaluating centroid moment tensor uncertainty in the new version of ISOLA software. Seism Res Lett 84: doi:10.1785/0220130002

Sokos E, Zahradník J, Kiratzi A, Janský J, Gallovič F, Novotný O, Kostelecký J, Serpetsidaki A, Tselentis GA (2012) The January 2010 Efpalio earthquake sequence in the western Corinth Gulf (Greece). Tectonophysics 530–531:299–309. doi:10.1016/j.tecto.2012.01.005

Zahradník J, Custódio S (2012) Moment tensor resolvability: application to southwest Iberia. Bull Seism Soc Am 102:1235–1254. doi:10.1785/0120110216

Zahradník J, Sokos E (2014) The Mw 7.1 Van, Eastern Turkey, earthquake 2011—two-point source modeling by iterative deconvolution and non-negative least squares. Geophys J Int 196:522–538. doi:10.1093/gji/ggt386